The HASHTAG project I. A survey of CO(3–2) emission from the star forming disc of M31

Zongnan Li [1,2]★ Zhiyuan Li [1,2]★ Matthew W. L. Smith [3]★ Christine D. Wilson [4]
Yu Gao,[5] Stephen A. Eales,[3] Yiping Ao,[5] Martin Bureau,[6,7] Aeree Chung,[8]
Timothy A. Davis [3] Richard de Grijs,[9,10,11] David J. Eden [12] Jinhua He,[13,14,15]
Tom M. Hughes [14,16,17,18] Xuejian Jiang [5] Francisca Kemper,[19,20]
Isabella Lamperti,[21] Bumhyun Lee [8] Chien-Hsiu Lee,[22] Michał J. Michałowski [23]
Harriet Parsons,[24] Sarah Ragan [3] Peter Scicluna [20] Yong Shi [1,2] Xindi Tang,[25]
Neven Tomičić,[26] Sebastien Viaene,[27,28] Thomas G. Williams [3] and Ming Zhu[29]

Affiliations are listed at the end of the paper

ABSTRACT

We present a CO(3–2) survey of selected regions in the M31 disc as part of the JCMT large programme, HARP and SCUBA-2 High-Resolution Terahertz Andromeda Galaxy Survey (HASHTAG). The 12 CO(3–2) fields in this survey cover a total area of 60 arcmin^2, spanning a deprojected radial range of 2–14 kpc across the M31 disc. Combining these observations with existing IRAM 30 m CO(1–0) observations and JCMT CO(3–2) maps of the nuclear region of M31, as well as dust temperature and star formation rate surface density maps, we are able to explore the radial distribution of the CO(3–2)/CO(1–0) integrated intensity ratio (R_{31}) and its relationship with dust temperature and star formation. We find that the value of R_{31} between 2 and 9 kpc galactocentric radius is 0.14, significantly lower than what is seen in the nuclear ring at 1 kpc ($R_{31} \sim 0.8$), only to rise again to 0.27 for the fields centred on the 10 kpc star forming ring. We also found that R_{31} is positively correlated with dust temperature, with Spearman's rank correlation coefficient $\rho = 0.55$. The correlation between star formation rate surface density and CO(3–2) intensity is much stronger than with CO(1–0), with $\rho = 0.54$ compared to -0.05, suggesting that the CO(3–2) line traces warmer and denser star forming gas better. We also find that R_{31} correlates well with star formation rate surface density, with $\rho = 0.69$.

Key words: ISM: molecules – galaxies: individual (M 31) – galaxies: ISM.

1 INTRODUCTION

Star formation is one of the key processes in galaxy formation and evolution. As stars are born in cold gas, the rate of star formation is thought to scale with the total amount of cold gas (i.e. molecular plus atomic gas) known as the Kennicutt–Schmidt law (KS law; Schmidt 1959; Kennicutt 1989; Kennicutt et al. 2007): $\Sigma_{SFR} \propto \Sigma_{gas}^{\alpha}$ with $\alpha \approx 1.4$, where Σ_{SFR} is the star formation rate (SFR) surface density and Σ_{gas} is the cold gas surface density. While atomic hydrogen can be directly detected through its 21 cm line, the H_2 molecule radiates weakly in rotational and vibrational states because it has no

permanent electric dipole moment. Thus, the rotational transition of carbon monoxide (CO) is usually used as a proxy for H_2, as it is the second most abundant molecule, and its luminosity is approximately proportional to the total molecular gas mass (Bolatto, Wolfire & Leroy 2013).

Recently, large surveys of nearby galaxies with advanced telescopes and instruments, including The HI Nearby Galaxy Survey (THINGS; Walter et al. 2008), the Key Insights on Nearby Galaxies: A Far-Infrared Survey with Herschel (KINGFISH; Kennicutt et al. 2011), the HERA CO-Line Extragalactic Survey (HERACLES; Leroy et al. 2009), and the JCMT Nearby Galaxies Legacy Survey (NGLS; Wilson et al. 2012), have enabled a detailed analysis of different gas components. These surveys revealed that the SFR surface density on and above a scale of a kiloparsec has a tighter correlation with the molecular gas surface density than with the
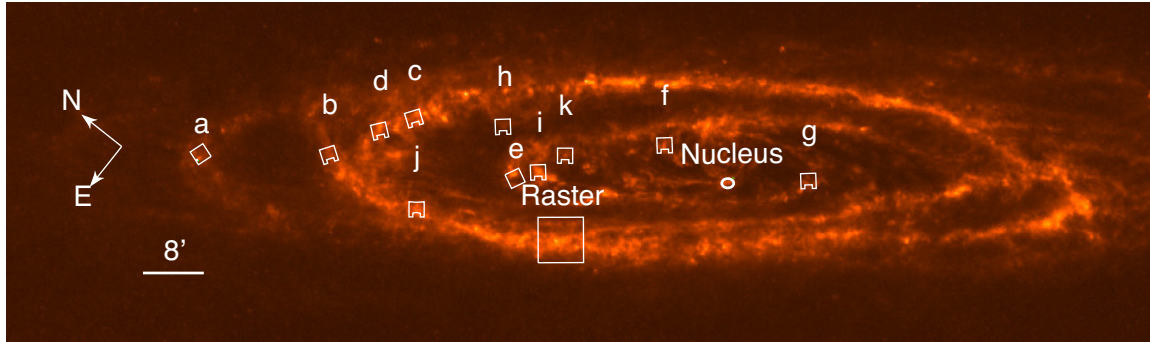
Figure 1. The footprint of the 11 HASHTAG jiggle fields (small white squares) and one raster field (large white box) overlaid on the Herschel/SPIRE 250 μm image of M31. The small ellipse labelled 'Nucleus' indicates a region on the nuclear ring studied by Li et al. (2019).

total gas surface density, with a power-law index close to unity (e.g. Bigiel et al. 2008, 2011; Leroy et al. 2008; Wilson et al. 2012). Despite the success on kpc scales, the behaviour of the KS law is still unclear below a scale of 500 pc, and a mystery below 100 pc (Viaene, Forbrich & Fritz 2018; Querejeta et al. 2019).

Galaxies in the Local Group provide a unique laboratory to study the interstellar medium (ISM) and star formation, thanks to their proximity. In particular, at a distance of 780 kpc (McConnachie et al. 2005; de Grijs & Bono 2014), where 1 arcsec ∼ 3.8 parsec, M31 provides a spatially resolved view of the ISM and star forming activities in a massive spiral. It is also a useful contrast to our own Galaxy because M31 has a more prominent classical bulge (the classification of this bulge is still under debate; e.g. Beaton et al. 2007; Saglia et al. 2018) and less prominent spiral arms than the Milky Way, with most of the current star formation occurring in the so-called 10 kpc ring (Gordon et al. 2006), which is likely a resonance phenomenon connected to the bulge and a weak bar (Lewis et al. 2015).

Previous surveys of CO(1–0) (Nieten et al. 2006) and HI (Braun et al. 2009) emission have revealed the global structure and kinematics of cold gas in M31. Observations of CO(2–1) lines towards several selected regions of M31 found the CO(2–1)/CO(1–0) intensity ratios to be 0.5–0.7 in the arms (Nieten et al. 2006) and close to unity in the central region (Melchior & Combes 2011), similar to the trend found in other disc galaxies. Despite the widespread use of CO(1–0) spectroscopy to trace the molecular gas, higher CO rotational transitions are needed to better constrain the molecular gas properties, in particular its excitation. The upper level energies of CO(1–0), CO(2–1), and CO(3–2) emission correspond to 5.5, 16.5, and 33.3 K, and the critical densities are $\sim 10^{3.5}$, $10^{4.3}$, and 10^5 cm^{-3}, respectively (Mao et al. 2010). In comparison, typical temperatures and densities of giant molecular clouds are ~ 10 K (Scoville & Sanders 1987) and 10^2–10^3 cm^{-3} (Solomon et al. 1987). Hence, compared with the two lower transitions of CO, CO(3–2) emission is a better tracer of warmer and denser gas that is more directly related to star formation (Muraoka et al. 2007; Wilson et al. 2009). Furthermore, the CO(3–2)/CO(1–0) ratio can trace the variation of physical conditions of the bulk molecular gas, which, in fact, has been proved to be a good indicator of gas temperature (Wilson, Walker & Thornley 1997) and density (e.g. Banerji, Viti & Williams 2009).

The dust temperature of M31 shows a general declining trend with galactocentric radius (e.g. Smith et al. 2012), and it is claimed that evolved stellar populations (a few Gyr old) are the primary heating source of dust, given that M31 is deficient in recent star formation activity (e.g. Montalto et al. 2009; Groves et al. 2012;

Viaene et al. 2017). Exploring the properties of the molecular gas in M31 could help determine whether M31 contains a large reservoir of very cold gas, and shed light on the relationship between gas and dust temperatures and the possible heating mechanisms.

Taking advantage of the sensitive instruments on the James Clerk Maxwell Telescope (JCMT), we are carrying out the HARP and SCUBA-2 High-Resolution Terahertz Andromeda Galaxy Survey (HASHTAG), which consists of dust continuum observations at 450 and 850 μm, and spectroscopic observations of the CO(3–2) line. The full HASHTAG survey, which will include SCUBA-2 observations of the entire disc of M31, is described in the survey paper (M. Smith et al., in preparation). This paper presents initial results from the HASHTAG CO(3–2) survey, which is the first systematic census of CO(3–2) emission in M31. In Section 2, we describe the CO(3–2) observations and data reduction. In Section 3, we present products including CO(3–2) spectra, integrated intensity maps, and the velocity field. We also investigate the CO(3–2)/CO(1–0) ratio in this section, based on which we address implications on the molecular gas properties. A summary is given in Section 4.

2 OBSERVATIONS AND DATA REDUCTION

2.1 HASHTAG CO(3–2) data

The HASHTAG CO(3–2) observations were carried out with the 16-pixel array receiver HARP-B instrument (Buckle et al. 2009) and the Auto-Correlation Spectrometer Imaging System (ACSIS) configured to have a bandwidth of 1 GHz and a resolution of 0.488 MHz, corresponding to 0.43 km s^{-1} at 345.796 GHz. The angular resolution of the JCMT at this frequency is 15 arcsec, with a pixel size of 7.5 arcsec in the processed images. We have observed eleven 2 arcmin × 2 arcmin ($\sim$500 pc × 500 pc) jiggle fields (labelled a–k in Fig. 1) and one 4 arcmin × 4 arcmin (1 kpc × 1 kpc) raster field, together covering selected star forming regions across the M31 disc. All observations were taken between 2017 July and October. During this time two receptors were not operational, causing gaps in almost all jiggle fields, except for JIGGLEa and JIGGLEe, where the gaps were filled in owing to receiver rotation. The integration time was 3.5 h for each of the 11 jiggle fields and 16.8 h for the raster field in band 3 weather (0.08 $< \tau_{225} <$ 0.12, where τ_{225} represents the 225 GHz opacity) to achieve a sensitivity of 17 mK (T_A^*, corrected antenna temperature) or better at a velocity resolution of 2.6 km s^{-1}. A log of the observations is given in Table 1.

Table 1. Observation Log.

Field	RA (J2000)	Dec (J2000)	PA (°)	Coverage (arcmin)	Integration time (h)	RMS (mK)	τ_{225}
JIGGLEa	00:46:31.0	+42:11:51.5	160.7	2 × 2	3.5	16.7	0.09
JIGGLEb	00:45:34.8	+41:58:28.5	145.7	2 × 2	3.5	13.7	0.10
JIGGLEc	00:44:37.2	+41:52:35.6	145.0	2 × 2	3.5	16.4	0.09
JIGGLEd	00:44:59.2	+41:55:10.5	141.0	2 × 2	3.5	14.6	0.09
JIGGLEe	00:44:26.5	+41:37:12.7	153.0	2 × 2	3.5	14.6	0.08
JIGGLEf	00:43:03.3	+41:24:16.2	130.0	2 × 2	3.5	15.9	0.10
JIGGLEg	00:42:21.4	+41:06:21.1	130.0	2 × 2	3.5	10.0	0.07
JIGGLEh	00:44:03.1	+41:42:39.3	130.0	2 × 2	3.5	13.8	0.09
JIGGLEi	00:44:13.2	+41:35:17.1	130.0	2 × 2	3.5	14.4	0.08
JIGGLEj	00:45:26.9	+41:44:54.6	37.7	2 × 2	3.5	13.6	0.09
JIGGLEk	00:43:52.2	+41:33:48.9	37.7	2 × 2	3.5	12.8	0.08
Raster	00:44:40.9	+41:27:25.2	37.7	4 × 4	16.8	14.5	0.08

Note. – (1) Field name. (2)–(4) Centres and position angles of these fields. (5) Coverage of the fields. (6) Total integration time of each field. (7) Mean RMS noise in T_A^*, measured at a velocity resolution of 2.6 km s^{-1}. (8) The 225 GHz opacity, representing the weather conditions.

Table 2. Line intensities and line ratios.

Field	$I_{CO(3-2)}$ [a]	$I_{CO(1-0)}$	$I_{CO(3-2)}/I_{CO(1-0)}$ [b]
JIGGLEa	0.50 ± 0.04	–	–
JIGGLEb	0.50 ± 0.03	1.89 ± 0.02	0.25 ± 0.02
JIGGLEc	1.02 ± 0.04	3.20 ± 0.08	0.29 ± 0.01
JIGGLEd	1.32 ± 0.04	4.46 ± 0.08	0.23 ± 0.01
JIGGLEe	1.00 ± 0.04	4.19 ± 0.17	0.21 ± 0.02
JIGGLEf	0.51 ± 0.03	4.93 ± 0.15	0.09 ± 0.01
JIGGLEg	0.19 ± 0.03	1.13 ± 0.05	0.15 ± 0.01
JIGGLEh	0.29 ± 0.02	2.82 ± 0.03	0.10 ± 0.01
JIGGLEi	0.81 ± 0.05	5.21 ± 0.10	0.14 ± 0.01
JIGGLEj	0.84 ± 0.04	3.18 ± 0.09	0.24 ± 0.01
JIGGLEk	0.73 ± 0.04	4.60 ± 0.13	0.14 ± 0.01
Raster	1.07 ± 0.04	2.95 ± 0.09	0.32 ± 0.01
Nucleus[c]	2.14 ± 0.22	2.38 ± 0.22	0.77 ± 0.10

Note. – [a] Mean integrated intensity of CO(3–2) in each field, in units of K km s^{-1}, with the statistical uncertainties at 1σ confidence level. [b] Mean ratio and uncertainty calculated using least-squares fitting method. [c] The intensities and line ratio of the nuclear ring.

The footprints of the observed fields are shown in Fig. 1. The fields were selected based on the following considerations: (1) Five fields (JIGGLEa–e) overlap with regions observed by Herschel imaging in [CII] 158 μm, [OI] 63 μm, and [NII] 122 μm and optical integral-field spectroscopy (Kapala et al. 2015); (2) in two fields (JIGGLEf, g), it has been suggested that there is a component of very cold gas (Allen & Lequeux 1993; Loinard et al. 1996; Loinard & Allen 1998); (3) four additional fields (JIGGLEh–k) have been covered by multiband optical imaging of the Panchromatic Hubble Andromeda Treasury (PHAT; Dalcanton et al. 2012), the CARMA CO(1–0) survey (Caldú-Primo & Schruba 2016; Schruba et al. in preparation) and IRAM CO(1–0)/CO(2–1) maps (Nieten et al. 2006), sampling a range of environments – the bulge, the inner ring, and the outer ring; (4) A 4 arcmin × 4 arcmin region on the 10 kpc ring, which we observed in raster mode (half-array spacing). In total, these 12 fields cover an area of 60 arcmin², spanning a projected radial range of 2–14 kpc across the M31 disc.

The data reduction follows the standard procedure for JCMT heterodyne observations, using the ORAC-DR pipeline (Jenness &

Economou 2015) based on the STARLINK software[1] (Currie et al. 2014). The pipeline automatically flagged spikes and bad detectors, subtracted linear baselines, and assessed data quality. However, after both automatically and manually flagging spectra with bad baselines, we noticed that one receptor remained questionable, which caused humps on the baselines in different fields. As the lines in our fields are relatively narrow (∼30 km s^{-1}) compared to the whole bandwidth (∼800 km s^{-1}), and the humps are relatively far away from the signal, we truncated the spectra down to 200 km s^{-1} wide to avoid the baseline noise caused by the humps.

We followed the methods described by Wilson et al. (2012) to obtain the moment maps. The main steps are summarized below. First, we shifted the velocity reference frame from HELIOCENTRIC (with respect to the sun) to kinematical Local Standard of Rest (LSRK) and divided each spectrum by the main-beam efficiency (η_{MB}) 0.64 to convert from antenna temperature to main-beam temperature. Then, we smoothed the CO(3–2) data cube to an angular resolution of 23 arcsec, corresponding to 88 pc in projection, and regridded the velocity resolution to 2.6 km s^{-1} to match the CO(1–0) survey data (Nieten et al. 2006; Section 2.2). Next, since the signal-to-noise ratio (S/N) of different fields varies due to different system temperatures, integration times, and unstable receptors, we divided the original data cubes by the noise maps produced using the line-free channels of each field to obtain the S/N cube.

We then applied the classical ClumpFind algorithm (Williams, de Geus & Blitz 1994) implemented as part of the STARLINK/CUPID task *findclumps* to the CO(3–2) data. By contouring the data and searching for the local maximum in the 3D S/N cubes, this algorithm identifies clumps with emission above three times the RMS noise and containing at least 50 pixels, with a pixel size of 7.5 arcsec (corresponding to ∼30 pc). Pixels that do not belong to any of the clumps are subsequently masked. Two (five) times the RMS noise was applied to the JIGGLEg and h (Raster) fields, since their signals are relatively weaker (stronger). The typical size (defined as the full width at half-maximum; FWHM) of the clumps is ∼90 pc, and the typical line width is 9 km s^{-1}. A list of the resultant clumps is given in the Appendix.

Taking advantage of the *findclumps* procedure, blended components along the line-of-sight were disentangled and identified as

---

[1] http://starlink.eao.hawaii.edu

different clumps. Application of this procedure has also improved the significance of the signal by eliminating the patchy local maxima that were much smaller than beam size which are most likely statistical fluctuations. Although there are a variety of clump finding algorithms that are also included in the CUPID package (GAUSSCLUMP, REINHOLD, and FELLWALKER; see Watson 2010, for a comprehensive assessment), the choice of specific algorithm does not significantly affect our conclusion, since our main goal is to find potentially coherent regions with sufficient S/N for analysis and comparison, but not to carry out a rigorous identification of individual molecular clouds. Moreover, we note that the detailed parameter selection of this algorithm has little influence on our results, as lowering the S/N cutoff or the pixel threshold can only add a few more clumps in total. Moment maps were created from the original data cube using the mask produced by *findclumps*.

2.2 Ancillary data

We used the CO(1–0) map from the IRAM 30 m survey presented by Nieten et al. (2006), which fully sampled an area of $2° \times 0.5°$ with an angular resolution of 23 arcsec. The mean RMS noise of the CO(1–0) integrated intensity map is $0.35 \, \mathrm{K \, km \, s^{-1}}$. We truncated the CO(1–0) image to match the fields of our observations using the *imregrid* task in CASA (McMullin et al. 2007), except for JIGGLEa which is at the far side of the disc and was not covered by the CO(1–0) survey. We then applied the same procedure as described in Section 2.1 to identify clumps and obtain moment maps of CO(1–0). Here we did not include the CO(2–1) data from the same survey, since those observations do not completely match our CO(3–2) fields, and the data are currently not available to us.

We also made use of a CO(3–2) map of the central $\sim 1 \, \mathrm{kpc}$ radius of M31 obtained in JCMT HARP raster mode (see the ellipse in Fig. 1; Li et al. 2019), taken with a resolution of 15 arcsec and a typical RMS of 3.5 mK in a $13 \, \mathrm{km \, s^{-1}}$ channel. Due to the general deficiency of molecular gas in this region, only a small portion of the so-called nuclear ring covered by our field-of-view has CO(1–0) detections, from which we can derive the CO(3–2)/CO(1–0) ratios (Li et al. 2019). Due to the shallower effective integration, the CO(3–2) RMS here is higher ($\sim 25 \, \mathrm{mK}$). These data complement the HASHTAG observations in terms of radial coverage.

The dust temperature map used here is from Smith et al. (2012) (Fig. 1), which is based on spectral energy distribution fitting of *Herschel* Photodetector Array Camera and Spectrometer (PACS) and Spectral and Photometric Imaging Receiver (SPIRE) 100, 160, 250, 350, and 500 μm observations along with *Spitzer* Multiband Imaging Photometer (MIPS) 70 μm data. A Bayesian method (PPMAP; Marsh, Whitworth & Lomax 2015) has been applied to increase the angular resolution of this map to 8 arcsec (Whitworth et al. 2019).

The SFR surface density map with an angular resolution of 6 arcsec is from Ford et al. (2013),[2] which is calibrated based on the *GALEX* far-ultraviolet (FUV) map of M31 (Thilker et al. 2005) and a *Spitzer* MIPS 24 μm (Gordon et al. 2006) map, using the method prescribed by Leroy et al. (2008). Ford et al. (2013) also used *GALEX* near-ultraviolet (NUV) and *Spitzer* Infrared Array Camera

(IRAC) 3.6 μm maps to correct for foreground stars and emission from old stellar populations, respectively. Recently, Lewis et al. (2017), using the PHAT data, suggested that the FUV plus 24 μm method underestimates the SFR by a factor of 2.3–2.5. Furthermore, Tomičić et al. (2019) used the extinction-corrected H α line of five kpc-sized fields in M31 (coinciding with the positions of the JIGGLE a-e fields) to calibrate the SFR, and claimed it is five times higher than derived by Ford et al. (2013). For consistency of cross-field comparison, we still adopt the SFR map from Ford et al. (2013), bearing in mind that in most of our fields the actual SFR may potentially shift up by $\sim 0.5 \, \mathrm{dex}$.

3 RESULTS

In this section, we focus on the CO(3–2) line measurements, in a close comparison with the CO(1–0) emission observed by the IRAM survey. We also address the immediate implications for the physical conditions of the molecular gas and star formation in the disc of M31.

3.1 Line characteristics and morphology of the molecular gas

The integrated intensity contours of CO(3–2) (black) and CO(1–0) (white) are contrasted with the *Herschel*/SPIRE 250 μm map in Figs 2 and 3. Identified clumps are labelled in these maps. In some cases, such as clumps 1 and 2 in the JIGGLEb field, two components superposed along the line-of-sight can be separated by their velocity channels. Since the clumps are labelled at their barycentres (i.e. values given in Table A1) rather than their peaks, some clumps with peculiar shapes may appear to deviate from the strongest peaks (e.g. in the JIGGLEi field). The CO(3–2) emission is in general coincident with the CO(1–0) and dust emission, with CO(3–2) being more compact. In some fields, such as JIGGLEf, g, and h, the CO(3–2) emission is relatively weak, and does not trace the dust emission well. This is understandable, because the JIGGLEf and g fields are suggested to contain very cold gas (Allen & Lequeux 1993; Loinard et al. 1996; Loinard & Allen 1998), and JIGGLEh samples the interarm region, where molecular gas may be scarce and star formation is inactive. It is also possible that the CO clump is aligned with the dust continuum that is not associated with it. The high inclination of M31 can project clouds in such a way that they appear close to each other.

The CO(3–2) line-of-sight velocity map of the Raster field is shown in the right-hand panel of Fig. 3. It is in agreement with the CO(1–0) velocity field and consistent with the rotation pattern of the M31 disc. The two blue-shifted patches at the lower left (labelled '7' and '21') seem inconsistent with the bulk rotation pattern, which could be due to projection of clouds at different distances or outflows with velocities on the order of tens of $\mathrm{km \, s^{-1}}$ on a scale of $\sim 100 \, \mathrm{pc}$. It will be interesting to explore the nature of these anomalous regions in future work.

For each field, we stacked the CO(3–2) spectra with peak S/N greater than 5 and CO(1–0) spectra from the same region as CO(3–2), and then divided them by the number of spectra. The averaged spectra of CO(3–2) (red) and CO(1–0) (black) of each field are shown in Fig. 4. Except for the JIGGLEa field without CO(1–0) observations, the two lines of the other 11 fields agree well with each other, both in central velocity and velocity dispersion (see also the Appendix). The presence of broad lines and multiple components in some fields indicates blending of clumps either along the line-of-sight or across the field-of-view. Despite this

---

[2]In order to compare the inclination corrected SFR density map with our uncorrected CO data, we divided this map by cos i, with the inclination angle of M31, $i = 77°$ (McConnachie et al. 2005), which was applied by Ford et al. (2013).
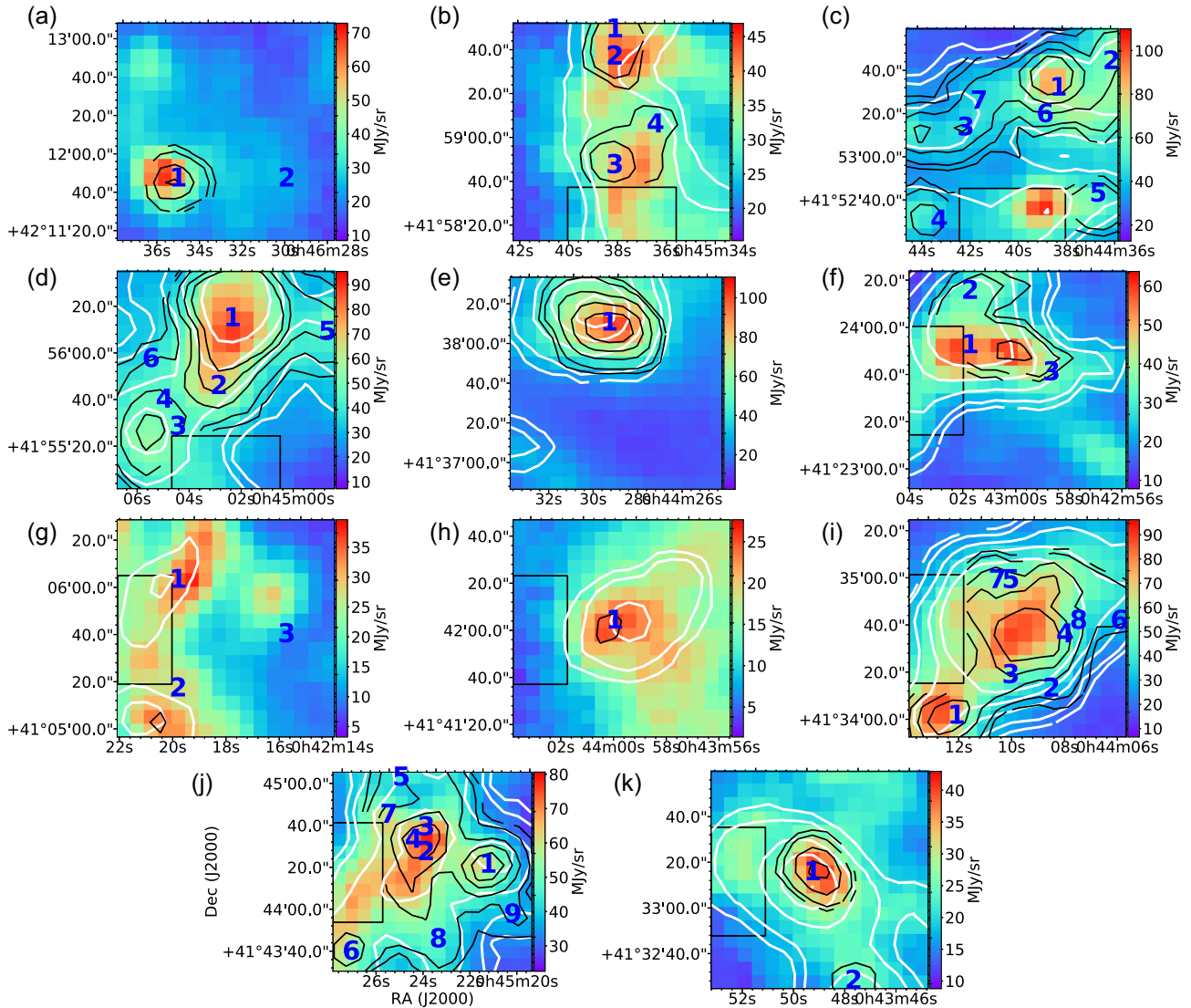
Figure 2. Herschel/SPIRE 250 μm maps of the 11 jiggle fields overlaid with CO(1–0) (white) and CO(3–2) integrated intensity contours (black). The contour levels correspond to 3, 5, 10, 15, 20σ, respectively, with 1σ level of 0.35 K km s^{-1} for CO(1–0) (Nieten et al. 2006), and 0.10 K km s^{-1} for CO(3–2), which is the typical rms noise in the integrated intensities. The physical scale of each field is approximately 500 pc in projection. Field 'a' had no CO(1–0) observation. The black rectangles indicate where there are no CO(3–2) observations due to the two receptors that are not operational. The clumps identified by ClumpFind are labelled with numbers. Note that in some cases two or more clumps lie in close proximity along the line-of-sight.

general agreement, there are a few fields with additional CO(1–0) components (JIGGLEc, e, k) or much broader CO(1–0) lines (JIGGLEh, i, and the Raster field). This could be the case if the corresponding CO(3–2) emission is too weak or absent along the line of sight. It is clear that in all fields the CO(3–2) lines are much weaker than the CO(1–0) lines.

3.2 CO(3–2)/CO(1–0) line ratios and gas properties

The CO(3–2)/CO(1–0) line ratio, R_{31}, has been suggested as a good indicator of temperature in the molecular gas, with higher ratios corresponding to higher temperatures (Wilson et al. 1997). It has also been suggested as an indicator of gas density (e.g. Banerji et al. 2009). Typical R_{31} values are found to be 0.4–0.5 in the disc of the Milky Way (Sanders et al. 1993; Oka et al. 2007), and similar values have been found in normal spiral galaxies, such as in NGC 4254 and NGC 4321 (Wilson et al. 2009), M51 (Vlahakis et al. 2013),

and NGC 628 (Muraoka et al. 2016). Comparison with these values could provide us with a deeper insight into the physical conditions of the molecular gas in M31.

To distinguish possible multiple components along the line of sight, we produced moment maps of individual clumps found by the ClumpFind algorithm as described in Section 2.1, from which we derived the integrated intensity, central velocity, and velocity dispersion of each spatial pixel in a given clump. We then identified the CO(3–2) and CO(1–0) lines of each pixel arising from the same clump if the difference of their central velocities is less than two channel widths (5.2 km s^{-1}) and both lines have velocity dispersions greater than one channel width (2.6 km s^{-1}). This selection excluded ~60 per cent of pixels with CO(1–0) detection but no CO(3–2) detection and ~7 per cent of pixels with CO(3–2) detection but no CO(1–0) detection, which is expected since CO(3–2) tends to probe the denser regions of molecular clouds. We provide the pixel-by-pixel velocity information of the two lines in the Appendix. The
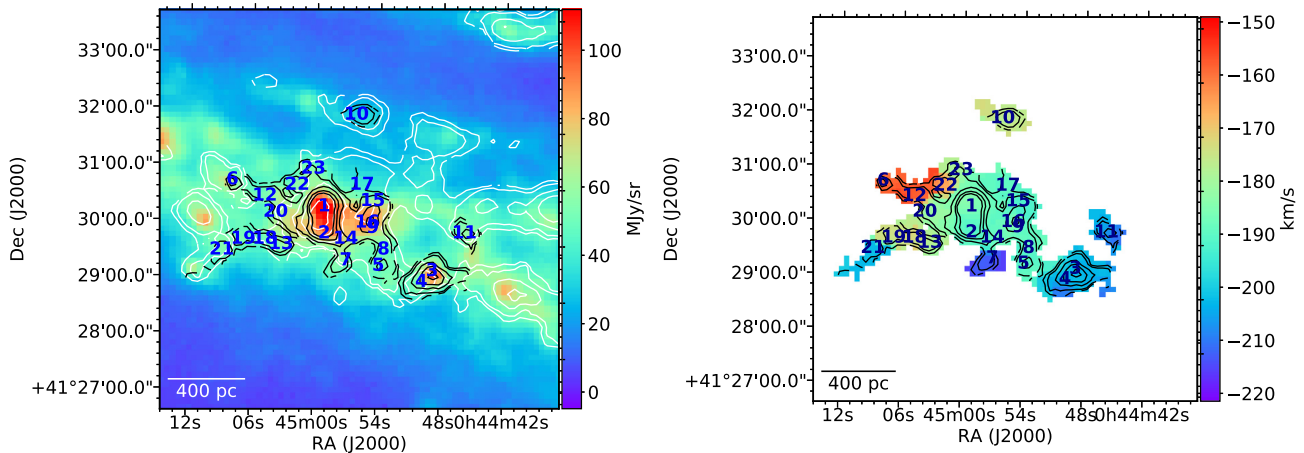
Figure 3. *Left-hand panel*: Herschel/SPIRE 250 μm maps of the raster field overlaid with CO(1–0) (white) and CO(3–2) integrated intensity contours (black), with contour levels as in Fig. 2. *Right-hand panel*: The CO(3–2) velocity field map of the raster field, overlaid with CO(3–2) contours. The clumps identified by ClumpFind are labelled with numbers.

following correlation analyses are based on the pixels thus selected. We note that these pixels are not fully independent. However, this should have little effect on our results as far as a global correlation is concerned.

Fig. 5 shows the pixel-by-pixel correlation of integrated intensities of the two lines. The measurement uncertainties in this plot are given by $\Delta T \times \Delta V \times \sqrt{N_{\mathrm{chan}}}$ (Wilson & Scoville 1989), where ΔT is the baseline RMS of each pixel, ΔV the channel width, and N_{chan} the number of channels used to produce the moment 0 maps. The uncertainties range from ∼1 per cent–30 per cent for CO(3–2) and ∼1 per cent–20 per cent for CO(1–0) in all fields, with an average value of ∼10 per cent and 5 per cent, respectively. The calibration uncertainties for CO(1–0) and CO(3–2) observations are not included here, which are 8 per cent (Saintonge et al. 2017) and 10 per cent,[3] respectively. They are taken into account in the line ratios calculated below.

There appears to be two branches in Fig. 5. The fields on the 10 kpc ring (with symbols in red-tinted colours) showing a higher CO(3–2) intensity with respect to CO(1–0), while other fields (symbols in blue-tinted colours) exhibit lower values in general. A few points with high line intensities ($I_{\mathrm{CO(3-2)}} > 3\,\mathrm{K\,km\,s^{-1}}$ and $I_{\mathrm{CO(1-0)}} > 6\,\mathrm{K\,km\,s^{-1}}$), belonging to either JIGGLEd or Raster, are spatially coincident with CO intensity peaks (e.g. clumps d1 and r1), which should trace dense molecular cores that might be the sites of active star formation. We applied linear regression to the CO(3–2) and CO(1–0) intensities, using the least-squares fitting method of the *kmpfit* module[4] in the Python package KAPTEYN, which accounts for uncertainties in both quantities, to obtain the mean CO(3–2)/CO(1–0) integrated intensity ratio (R_{31}). We found that the mean R_{31} values of the five fields on the 10 kpc ring (JIGGLEb, c, d, j, and the Raster field) and other fields (JIGGLEe, f, g, h, i, k) are 0.274 ± 0.005 and 0.137 ± 0.005, respectively, which are indicated as black lines in Fig. 5. The average line ratio derived from the 11 fields (JIGGLEa has no corresponding CO(1–0) observations) in the disc is 0.228 ± 0.004. For comparison, the black data points are from the nuclear region (Li et al. 2019), which shows a substantially

higher line ratio of 0.77 ± 0.10. We also calculated the mean R_{31} for each field using the same least-squares fitting method. The results are given in Table 2 and shown as colour-coded dotted lines in Fig. 5. Note that the R_{31} values of the JIGGLEg and h fields are calculated from the 'peak' region with CO(3–2) emission, as the CO(1–0) emission is spatially more extended (Fig. 2), hence these values cannot represent the line ratio of the whole field. Combining the measurements of R_{31} in the central kpc obtained by Li et al. (2019), Fig. 6 illustrates the distribution of R_{31} as a function of the deprojected galactocentric radius. It is clear that the nuclear ring exhibits the highest value of R_{31} (∼0.8), while the 10 kpc ring shows on average a higher line ratio (∼0.27) than the inner disc regions (∼0.14).

We performed radiation transfer calculations of line ratios using the RADEX code (van der Tak et al. 2007) to constrain the coupled gas kinetic temperature T_k and volume density of molecular hydrogen $n_{\mathrm{H_2}}$, allowing for optically thick conditions. We adopted the large velocity gradient (LVG) approximation model (e.g. Goldreich & Kwan 1974; Scoville & Solomon 1974), which is widely used in the analysis of molecular lines, given the fact that thermal line broadening is far smaller than the velocity dispersion within clouds. The calculations span kinetic temperature $T_k = 5$–50 K and molecular hydrogen density $n_{\mathrm{H_2}} = 10^2$–$10^4\,\mathrm{cm^{-3}}$. For the CO column density (N_{CO}) and velocity gradient (dv), we followed Koda et al. (2012) to use a typical $\log(N_{\mathrm{CO}}/\mathrm{d}v\,(\mathrm{cm^{-2}/(km\,s^{-1}))}) = 16.6$–17.3 based on the observed line widths and assuming a standard ISM CO/H$_2$ abundance of 8×10^{-5} (Schinnerer et al. 2010). There are a number of caveats pertaining to this analysis that should be kept in mind before interpreting the results. First, the uncertainty in the CO/H$_2$ abundance is not taken into account in the calculations. Moreover, with only two lines, the constraints given by the RADEX code are undetermined and limited. Nevertheless, Fig. 7 shows the calculation results for $R_{31} = 0.14, 0.27, 0.77$, with solid and dashed curves representing $\log(N_{\mathrm{CO}}/\mathrm{d}v) = 16.6$ and 17.3, respectively. In this plot, the higher R_{31} ratio indicates both higher temperature and higher density in general, with the highest mean ratio of the nuclear region, 0.77, requiring a temperature $\gtrsim 20$ K and density $\gtrsim 10^{3.5}\,\mathrm{cm^{-3}}$, while the lowest value 0.14 only requiring a kinetic temperature $\gtrsim 5$ K.

According to the LVG results, the high line ratio in the nuclear region could be due to a high kinetic temperature or a high volume density (or both). However, the low line-of-sight dust extinction

[3]https://www.eaobservatory.org/jcmt/instrumentation/heterodyne/calibration/
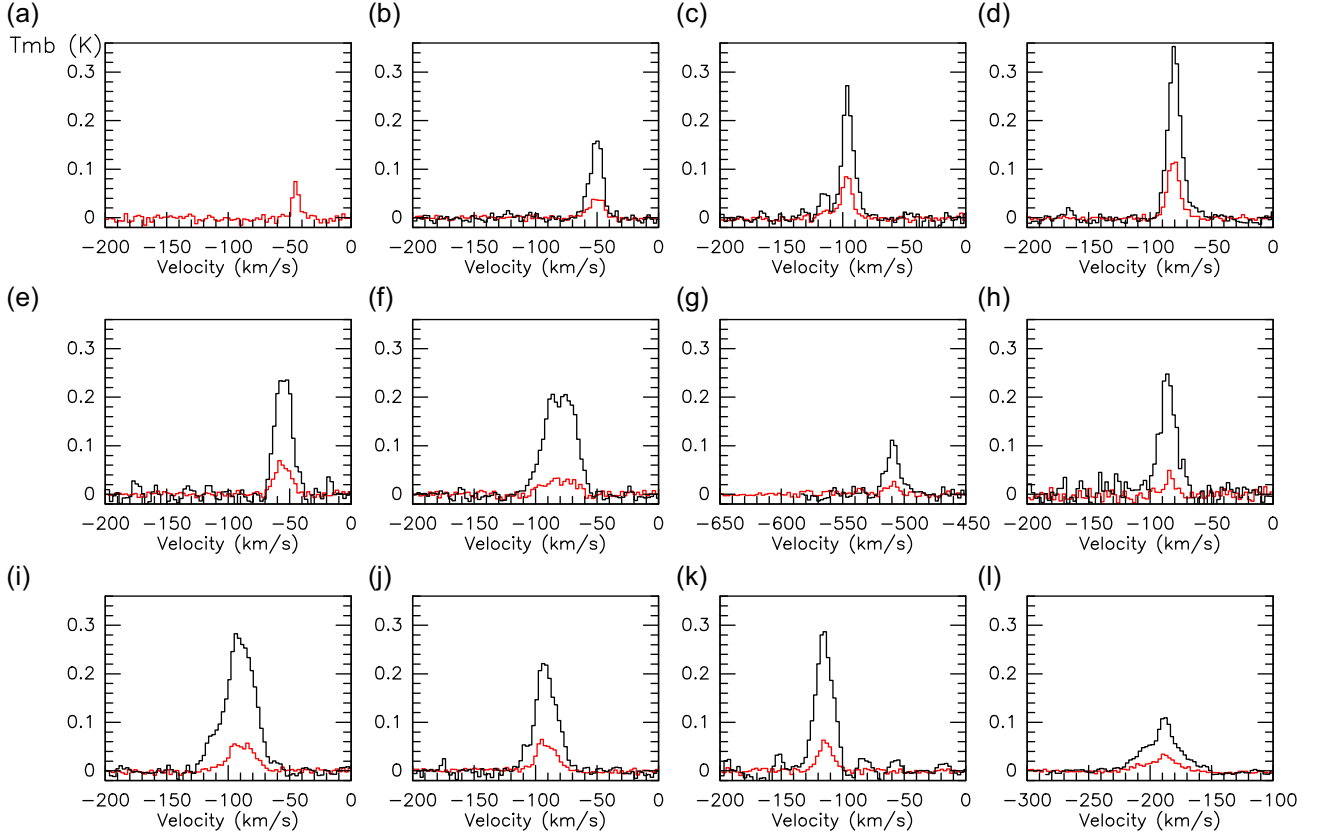[4]https://www.astro.rug.nl/software/kapteyn/kmpfit.html

Figure 4. The CO(3–2) (red) and CO(1–0) (black) line profiles of the 12 fields, averaged using CO(3–2) spectra with peak S/N > 5 and CO(1–0) spectra from the same region. Field 'a' was not covered in CO(1–0) by the survey of Nieten et al. (2006).
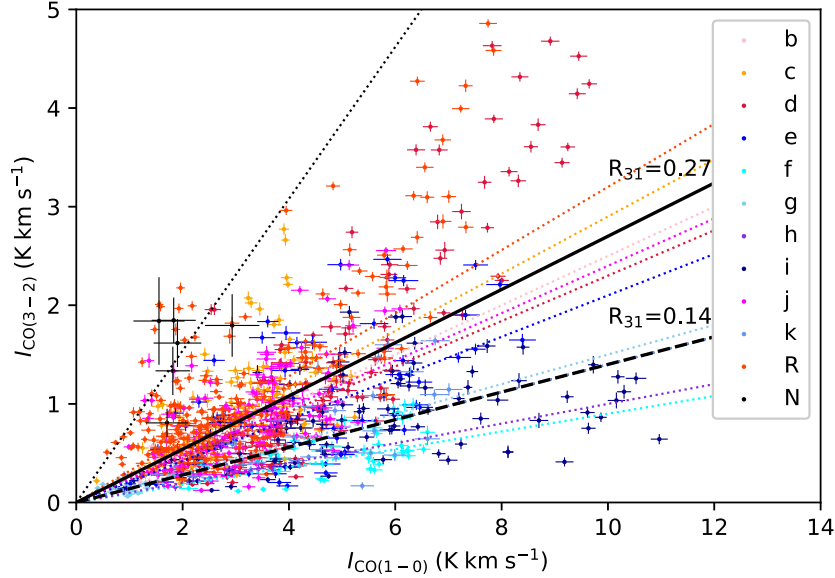

Figure 5. The pixel-by-pixel correlation of the integrated intensity of the 12 HASHTAG fields, plus the additional Nucleus field (denoted by 'N') studied by Li et al. (2019). Each pixel is obtained from the moment maps based on individual clumps found by ClumpFind and selected using the criteria described in Section 2.1. Only the measurement uncertainties are shown in the plot. The red-tinted points represent the fields in the 10 kpc ring, with the solid line indicating their mean CO(3–2)/CO(1–0) line ratio, 0.27, while the blue-tinted points are from the other fields in the disc, with the dashed line representing their mean line ratio of 0.14. The colour-coded dotted lines indicate the mean line ratios for each field, as listed in Table 2.
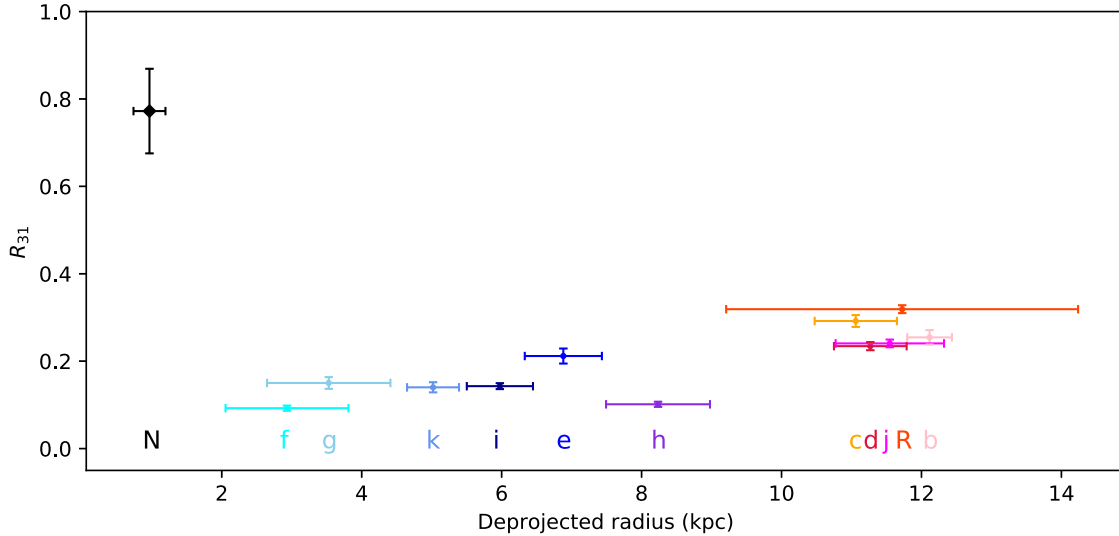
Figure 6. The radial distribution of CO(3–2)/CO(1–0) intensity ratio, derived from the 11 HASHTAG fields (circles) as well as from a segment of the nuclear ring (diamond, labelled 'N'; Li et al. 2019), same as in Table 2. The deprojected radius is calculated assuming position angle 38° and an inclination angle of 77° for the disc (McConnachie et al. 2005). For the nuclear ring, the inclination angle is assumed to be 45° (Ciardullo et al. 1988). The vertical and horizontal error bars represent the uncertainty of the fitted ratio and the radial coverage of each field, respectively.
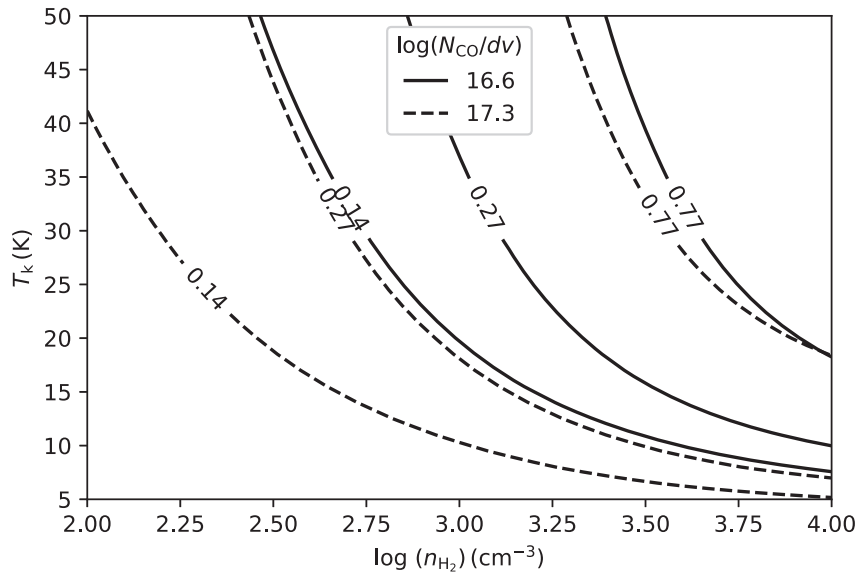

Figure 7. LVG calculation results for R_{31} = 0.14, 0.27, 0.77, with solid and dashed curves representing $\log(N_{CO}/dv \ (\mathrm{cm^{-2}/(km\ s^{-1})}))$ = 16.6 and 17.3, respectively, which can reproduce the observed line ratios of most HASHTAG fields assuming a CO abundance with respect to H_2 of 8×10^{-5}.

towards the M31 centre (Li, Wang & Wakker 2009; Dong et al. 2016) indicates the general absence of very dense and massive molecular clouds. Thus, it is more likely that high temperature is the dominant factor here. This demands heating mechanisms other than star formation or active galactic nucleus (AGN), given the absence of massive stars and nuclear activity in the centre of M31 (Li et al. 2011). One possibility is heating by old stellar populations that have been claimed to heat the dust in the nuclear region (e.g. Montalto et al. 2009). Meanwhile, the relatively high line ratio of the five fields on the 10 kpc ring (∼0.27) indicates a higher temperature and/or density compared to the inner disc region. This could be due to the difference in star formation activity, since the 10 kpc ring is actively forming stars, while the rest of the disc is quiescent. Among the fields in the inner disc, JIGGLEe has the highest line ratio of

0.21, which may be due to its moderate star formation activity as evidenced by the HII regions therein (Kapala et al. 2015). Two fields (JIGGLEf, g) have been previously suggested to contain very cold gas (Allen & Lequeux 1993; Loinard et al. 1996; Loinard & Allen 1998); although their R_{31} values are indeed low (0.09 and 0.15), these values are comparable to those of other fields in the inner disc (such as JIGGLE h, i, k). The fact that the R_{31} ratio in M31's disc (∼0.23) is lower than that of the Milky Way disc (∼0.4; Oka et al. 2012) may suggest that the molecular gas of the M31 disc is on average colder, consistent with the overall low SFR in M31.

The dust temperature in M31 follows a negative correlation with radius, that is, close to ∼30 K in the central region and rapidly decreasing to ∼17 K beyond 3 kpc (e.g. Smith et al. 2012; Draine et al. 2014). In Fig. 8, we contrast R_{31}, a plausible indicator
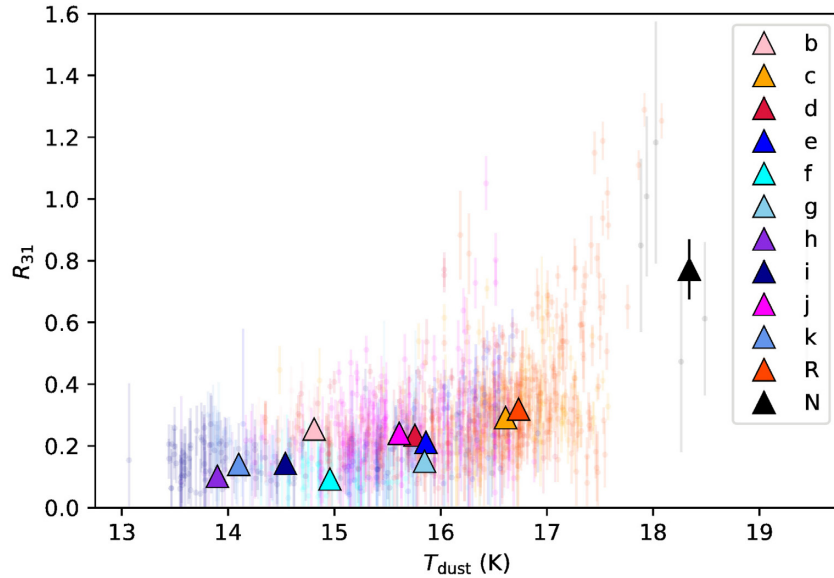
Figure 8. R_{31} versus dust temperature of each pixel (dots), overlaid with average values of each field (triangles).

of molecular gas temperature, with the dust temperature (Smith et al. 2012) on a pixel-by-pixel basis for a common resolution of 23 arcsec. To evaluate a possible correlation, we computed the Spearman's rank correlation coefficient ρ, which is 0.554 for the whole data set. The p-value, defined as the probability under the null hypothesis of random variables, is <0.001. Even after removing data from the nuclear ring, the rank coefficient ρ only decreases a little to 0.546, with p-value < 0.001. The results suggest a positive correlation between R_{31} and dust temperature indeed exists. This correlation could be an implication of the relationship between gas and dust temperature, as R_{31} is a good indicator of gas temperature.

3.3 Correlation with star formation rate

Previous studies have shown that CO(3–2) emission is more tightly related to star formation than CO(1–0), exhibiting a nearly linear correlation with SFR (e.g. Komugi et al. 2007; Muraoka et al. 2007; Wilson et al. 2009). Similarly, Wilson et al. (2012) compared the CO(3–2) luminosity of the NGLS sample with the far-infrared luminosity from the *Spitzer* Infrared Nearby Galaxies Survey (SINGS), finding that they are nearly linearly correlated. As for M31, Leroy et al. (2008), Ford et al. (2013), and Rahmani, Lianou & Barmby (2016) have claimed that the relationship between the SFR surface density (Σ_{SFR}) and the gas column density (Σ_{mol}; i.e. the KS law) varies radially in M31, the first time that such a radial variation was reported for a galaxy. Furthermore, they found a sublinear relationship between Σ_{SFR} and Σ_{mol} using the CO(1–0) survey data, which indicates the presence of CO-bright regions that are not efficiently forming stars.

We examined the relationship between the CO emission and the SFR surface density of Ford et al. (2013). The latter was convolved to a common resolution of 23 arcsec, with a typical uncertainty of $2.4 \times 10^{-4}\ M_\odot\ \mathrm{yr}^{-1}\ \mathrm{kpc}^{-2}$. Since the commonly used conversion factor $\alpha_{CO} = \Sigma_{mol}/I_{CO(1-0)}$ (Bolatto et al. 2013) is of substantial uncertainty (Shetty et al. 2011; Clark & Glover 2015), and there is no single factor for CO(3–2) to apply, we investigated the relationship among SFR surface density, Σ_{SFR}, and CO integrated intensity, I_{CO}, instead of the molecular gas surface density. As shown in Fig. 9(a), the relationship is examined pixel-by-pixel (small dots), overlaid

with the mean values of each field (triangles) on a characteristic scale of ∼500 pc.

The correlation between the SFR surface density and CO(3–2) integrated intensity for the 12 HASHTAG fields is relatively strong, with Spearman's rank correlation coefficient $\rho = 0.54$ (p < 0.001). We thus fitted a linear relationship between them on a pixel-by-pixel basis, using the Markov chain Monte Carlo (MCMC) method implemented in the Python package EMCEE (Foreman-Mackey et al. 2013), following Sun et al. (2018). We found a best-fitting power-law index $0.49^{+0.03}_{-0.03}$, as shown by the black strip in Fig. 9(a). This index is roughly consistent with that found by Rahmani et al. (2016) in their analysis of H_2-only gas, based on CO(1–0) conversion, which is 0.540 ± 0.003 for the whole galaxy. However, it is still lower than that reported by both Tabatabaei & Berkhuijsen (2010) (∼1.0) and Ford et al. (2013) (∼0.6). We note that the JIGGLE h and k fields have much lower SFR surface densities than the other fields ($< 10^{-3}\ M_\odot\ \mathrm{yr}^{-1}\ \mathrm{kpc}^{-2}$); both lie in the interarm region where little star formation is observed. If we were to exclude these two fields as outliers, the power-law index will become even lower, 0.46 ± 0.02. Therefore, the selection criteria of data points, such as the choice of outliers and an S/N cut (Williams, Gear & Smith 2018), may affect the power-law index. For comparison, Williams et al. (2018) found a superlinear correlation between Σ_{SFR} and Σ_{H_2} in M33 on a similar sub-kpc scale. This suggests that the KS law may vary substantially from one galaxy to another, as claimed by Shetty, Kelly & Bigiel (2013).

On the other hand, the CO(1–0) emission from the HASHTAG fields shows no significant correlation with the SFR surface density, with rank coefficient $\rho = -0.05$ (p = 0.16). This may be explained by our limited number of data points compared with other studies, and the relation we discussed here is all based on small regions with characteristic sizes $\lesssim 500$ pc, where the relation may not hold (Tabatabaei & Berkhuijsen 2010; Ford et al. 2013; Querejeta et al. 2019). On small scales, other factors than the molecular gas surface density may play a key role in determining the star formation activity (Bigiel et al. 2008; Leroy et al. 2008), such as gas turbulence (Sun et al. 2018) and stellar mass surface density (Shi et al. 2018).

We also examined the correlation between R_{31} and the SFR surface density, as shown in Fig. 9(c). The Spearman's coefficient
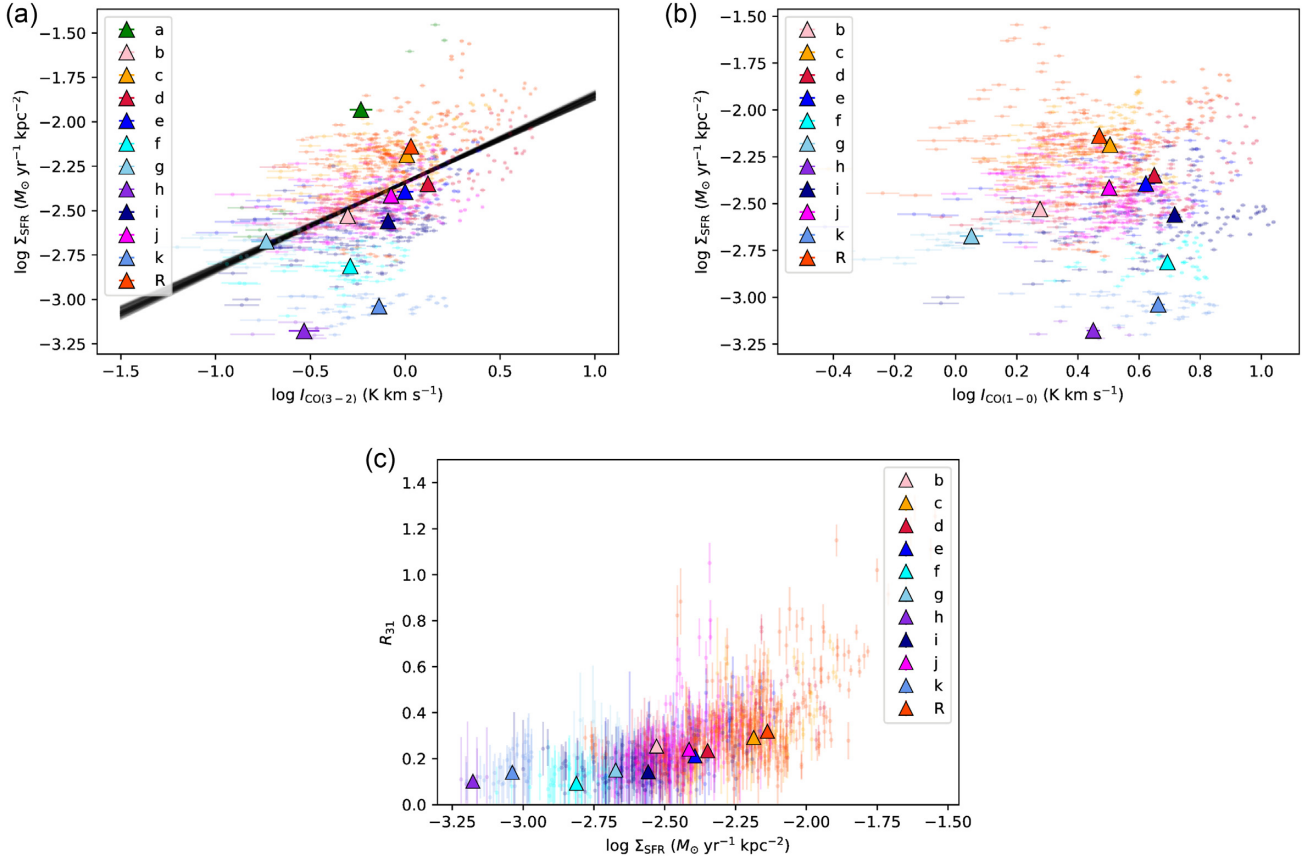
Figure 9. (a) Pixel-by-pixel (small dots) correlation of SFR surface density and CO(3–2) integrated intensity. The triangles represent the mean values of each field. The black strip represent a best-fitting power-law index of $0.49^{+0.03}_{-0.03}$. (b) Comparison of SFR surface density and CO(1–0) integrated intensity, with symbols the same as in (a). (c) Comparison of R_{31} ratio and SFR surface density Σ_{SFR} of each pixel (dot) and field (triangle).

for this correlation is 0.69 (p < 0.001), suggesting a significant correlation between SFR and R_{31}. Interestingly, Viaene et al. (2018) found a significant correlation between the SFR and HCN line emission, a commonly used tracer of dense gas (Gao & Solomon 2004), in a few individual giant molecular clouds of M31; they found an even tighter correlation between the SFR and the HCN/CO(1–0) ratio, which led them to propose a dependence of the SFR on the dense gas or dense gas fraction. Since CO(3–2) is sensitive to warm and dense gas, the relatively tight correlations between the SFR and the CO(3–2) intensity as well as the CO(3–2)/CO(1–0) ratio may suggest a dependence of the SFR on the warm gas density or warm gas fraction as well. It is noteworthy that almost all the points in the upper right part of Fig. 9(c) are from the 10 kpc star forming ring (the JIGGLEc, j and Raster fields), with higher line ratio, higher SFR surface density, and also, higher dust temperature. Thus, we suggest that the systematically higher values of R_{31} in the 10 kpc ring, compared to the inner disc, are at least partly due to star formation heating. Indeed, according to Viaene et al. (2017), the overall dust heating in M31 is dominated by evolved (i.e. old) stellar populations. However, the relative contributions of young stellar populations (i.e. younger than 100 Myr) in certain regions along the 10 kpc ring can be as high as 20 per cent–50 per cent, compared with the global fraction of 10 per cent.

4 SUMMARY

We have presented a systematicDD survey of CO(3–2) emission lines from 12 selected regions across the M31 disc, observed as part of the HASHTAG programme. The data will be publicly available

on the HASHTAG website.[5] We use these data as well as existing CO(3–2) and CO(1–0) observations and complementary multiwavelength images to investigate the properties of the molecular gas and its relation with dust and star formation activity in regions spanning a galactocentric radial range of 1–14 kpc. The main results are as follows:

(i) Except for JIGGLEa which lies at the far side of the disc and was not covered by the CO(1–0) survey, the CO(3–2) lines of all other 11 fields are much weaker than the CO(1–0) lines. We found that the R_{31} ratio of the M31 disc slightly increases with radius, from ∼0.14 within 10 kpc to ∼ 0.27 in the 10 kpc ring, while the ratio of the nuclear ring (at ∼1 kpc), ∼0.8, is significantly higher.

(ii) We conducted LVG calculations to reproduce the line ratios in the n_{H_2} and T_k plane, which requires higher kinetic temperature and volume density for higher line ratios in general. In the star forming 10 kpc ring, the higher line ratio may be explained by heating induced by star formation activity. Nevertheless, the high ratio and implied high temperature of the nuclear ring needs other heating mechanisms given the lack of nuclear star formation and AGN activity in M31. We also found a weak positive correlation between the dust temperature and the R_{31} ratio.

(iii) We also investigated the relation between Σ_{SFR} and I_{CO} of CO(3–2) and CO(1–0), respectively. We found a tighter relationship between the SFR surface density and CO(3–2) integrated intensity than with CO(1–0), consistent with previous studies. We also found a significant correlation with R_{31} and Σ_{SFR}.

[5] https://www.eao.hawaii.edu/HASHTAG

In this paper, we have focused on presenting the results of the CO(3–2) observations, and analyses of the R_{31} ratio. More in-depth investigation of the properties of cold ISM across the M31 disc, combining HASHTAG observations and complementary multiwavelength data, including *Herschel*, PHAT imaging, and other CO transitions, will be the subject of future work.

REFERENCES

Allen R. J., Lequeux J., 1993, ApJ, 410, L15
Banerji M., Viti S., Williams D. A., 2009, ApJ, 703, 2249
Beaton R. L., et al., 2007, ApJ, 658, L91
Bigiel F., Leroy A., Walter F., Brinks E., de Blok W. J. G., Madore B., Thornley M. D., 2008, AJ, 136, 2846
Bigiel F., et al., 2011, ApJ, 730, L13
Bolatto A. D., Wolfire M., Leroy A. K., 2013, ARA&A, 51, 207
Braun R., Thilker D. A., Walterbos R. A. M., Corbelli E., 2009, ApJ, 695, 937
Buckle J. V., et al., 2009, MNRAS, 399, 1026
Caldú-Primo A., Schruba A., 2016, AJ, 151, 34
Ciardullo R., Rubin V. C., Ford W. K., Jr., Jacoby G. H., Ford H. C., 1988, AJ, 95, 438
Clark P. C., Glover S. C. O., 2015, MNRAS, 452, 2057

Currie M. J., Berry D. S., Jenness T., Gibb A. G., Bell G. S., Draper P. W., 2014, in Manset N., Forshay P., eds, ASP Conf. Ser. Vol. 485, Astronomical Data Analysis Software and Systems XXIII. Astron. Soc. Pac., San Francisco, p. 391
Dalcanton J. J., et al., 2012, ApJS, 200, 18
de Grijs R., Bono G., 2014, AJ, 148, 17
Dong H., Li Z., Wang Q. D., Lauer T. R., Olsen K. A. G., Saha A., Dalcanton J. J., Groves B. A., 2016, MNRAS, 459, 2262
Draine B. T. et al., 2014, ApJ, 780, 172
Ford G. P. et al., 2013, ApJ, 769, 55
Foreman-Mackey D., Hogg D. W., Lang D., Goodman J., 2013, PASP, 125, 306
Gao Y., Solomon P. M., 2004, ApJ, 606, 271
Goldreich P., Kwan J., 1974, ApJ, 189, 441
Gordon K. D. et al., 2006, ApJ, 638, L87
Groves B. et al., 2012, MNRAS, 426, 892
Jenness T., Economou F., 2015, Astron. Comput., 9, 40
Kapala M. J. et al., 2015, ApJ, 798, 24
Kennicutt R. C., 1989, ApJ, 344, 685
Kennicutt R. C. et al., 2007, ApJ, 671, 333
Kennicutt R. C., et al., 2011, PASP, 123, 1347
Koda J. et al., 2012, ApJ, 761, 41
Komugi S., Kohno K., Tosaki T., Nakanishi H., Onodera S., Egusa F., Sofue Y., 2007, PASJ, 59, 55
Leroy A. K., Walter F., Brinks E., Bigiel F., de Blok W. J. G., Madore B., Thornley M. D., 2008, AJ, 136, 2782
Leroy A. K. et al., 2009, AJ, 137, 4670
Lewis A. R. et al., 2015, ApJ, 805, 183
Lewis A. R. et al., 2017, ApJ, 834, 70
Li Z., Wang Q. D., Wakker B. P., 2009, MNRAS, 397, 148
Li Z., Garcia M. R., Forman W. R., Jones C., Kraft R. P., Lal D. V., Murray S. S., Wang Q. D., 2011, ApJ, 728, 10
Li Z., Li Z., Zhou P., Gao Y., Jiang X.-J., Dong H., 2019, MNRAS, 484, 964
LoinardL., Allen R. J., Lequeux J., 1996, A&A, 310, 93
LoinardL., Allen R. J., 1998, ApJ, 499, 227
Mao R.-Q., Schulz A., Henkel C., Mauersberger R., Muders D., Trung D.-V., 2010, ApJ, 724, 1336
Marsh K. A., Whitworth A. P., Lomax O., 2015, MNRAS, 454, 4282
McConnachie A. W., Irwin M. J., Ferguson A. M. N., Ibata R. A., Lewis G. F., Tanvir N., 2005, MNRAS, 356, 979
McMullin J. P., Waters B., Schiebel D., Young W., Golap K., 2007, in Shaw R. A., Hill F., Bell D. J., eds, ASP Conf. Ser. Vol. 376, Astronomical Data Analysis Software and Systems XVI. Astron. Soc. Pac., San Francisco, CA, p. 127
Melchior A. L., Combes F., 2011, A&A, 536, A52
Montalto M., Seitz S., Riffeser A., Hopp U., Lee C. -H., Schönrich R., 2009, A&A, 507, 283
Muraoka K. et al., 2007, PASJ, 59, 43
Muraoka K. et al., 2016, PASJ, 68, 18
Nieten Ch., Neininger N., Guélin M., Ungerechts H., Lucas R., Berkhuijsen E. M., Beck R., Wielebinski R., 2006, A&A, 453, 459
Oka T., Nagai M., Kamegai K., Tanaka K., Kuboi N., 2007, PASJ, 59, 15
Oka T., Onodera Y., Nagai M., Tanaka K., Matsumura S., Kamegai K., 2012, ApJS, 201, 14
Querejeta M. et al., 2019, A&A, 625, A19
Rahmani S., Lianou S., Barmby P., 2016, MNRAS, 456, 4128
Saglia R. P., Opitsch M., Fabricius M. H., Bender R., Blana M., Gerhard O., 2018, A&A, 618, A156
Saintonge A. et al., 2017, ApJS, 233, 22
Sanders D. B., Scoville N. Z., Tilanus R. P. J., Wang Z., Zhou S., 1993, in Holt S. S., Verter F., eds, AIP Conf. Proc. Vol. 278, Back to the Galaxy. Am. Inst. Phys., New York, p. 311
Schinnerer E., Weiß A., Aalto S., Scoville N. Z., 2010, ApJ, 719, 1588
Schmidt M., 1959, ApJ, 129, 243
Scoville N. Z., Sanders D. B., 1987, in Hollenbach D. J., Thronson H. A., Jr., eds, Astrophysics and Space Science Library, Vol. 134, Interstellar Processes. Reidel, Dordrecht, p. 21
Scoville N. Z., Solomon P. M., 1974, ApJ, 187, L67

Shetty R., Glover S. C., Dullemond C. P., Ostriker E. C., Harris A. I., Klessen R. S., 2011, MNRAS, 415, 3253

Shetty R., Kelly B. C., Bigiel F., 2013, MNRAS, 430, 288

Shi Y. et al., 2018, ApJ, 853, 149

Smith M. W. L. et al., 2012, ApJ, 756, 40

Solomon P. M., Rivolo A. R., Barrett J., Yahil A., 1987, ApJ, 319, 730

Sun J. et al., 2018, ApJ, 860, 172

Tabatabaei F. S., Berkhuijsen E. M., 2010, A&A, 517, A77

Thilker D. A., et al., 2005, ApJ, 619, L67

Tomičić N. et al., 2019, ApJ, 873, 3

van der Tak F. F. S., Black J. H., Schöier F. L., Jansen D. J., van Dishoeck E. F., 2007, A&A, 468, 627

Viaene S. et al., 2017, A&A, 599, A64

Viaene S., Forbrich J., Fritz J., 2018, MNRAS, 475, 5550

Vlahakis C., van der Werf P., Israel F. P., Tilanus R. P. J., 2013, MNRAS, 433, 1837

Walter F., Brinks E., de Blok W. J. G., Bigiel F., Kennicutt R. C., Thornley M. D., Leroy A. K., 2008, AJ, 136, 2563

Watson M. E., 2010, Master's thesis, University of Hertfordshire

Whitworth A. P. et al., 2019, MNRAS, 489, 5436

Williams J. P., de Geus E. J., Blitz L., 1994, ApJ, 428, 693

Williams T. G., Gear W. K., Smith M. W. L., 2018, MNRAS, 479, 297

Wilson C. D., Scoville N., 1989, ApJ, 347, 743

Wilson C. D., Walker C. E., Thornley M. D., 1997, ApJ, 483, 210

Wilson C. D. et al., 2009, ApJ, 693, 1736

Wilson C. D. et al., 2012, MNRAS, 424, 3050

APPENDIX A:

The pixel-by-pixel comparison of the line-of-sight velocity and velocity dispersion between the CO(3–2) and CO(1–0) lines, after applying the criteria described in Section 3.2, is shown in Fig. A1. Different velocity components of each field are evident in the top panel, and it is clear that the two lines have a consistent velocity dispersion despite the large scatter.

We list the 69 clumps found with the CLUMPFIND algorithm in *findclump* task in Table A1. They are listed in order of the field name. For example, clump 'a1' is the first clump found in JIGGLEa field. Their positions, sizes, peak, and integrated intensities are given in the table. The clumps have a typical size (FWHM) of ∼90 pc, and a typical line width of ∼9 km s^{-1}.
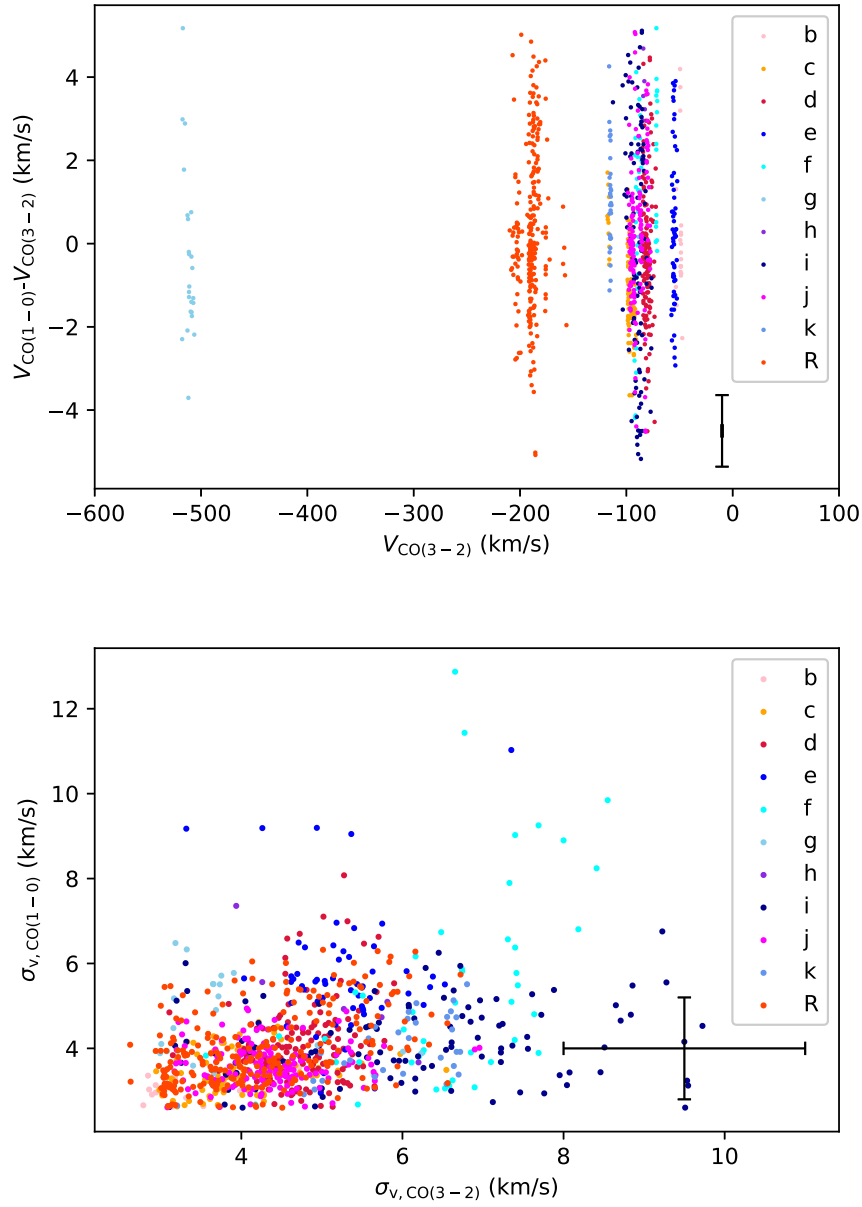
Figure A1. Pixel-by-pixel comparison of the line-of-sight velocity (top panel) and velocity dispersion (bottom panel) between CO(3–2) and CO(1–0) in all HASHTAG fields. Each pixel is obtained from the moment maps based on individual clumps found by ClumpFind. We only consider the two lines to arise from the same component if the difference of their central velocity is less than two channel widths, $5.2\,\mathrm{km\,s^{-1}}$. We also eliminated pixels with velocity dispersion narrower than the channel width $2.6\,\mathrm{km\,s^{-1}}$. The typical uncertainty is shown as black cross at the lower right.

Table A1. Catalogue of identified molecular clumps.

ID	RA (J2000) (°)	Dec (J2000) (°)	v (km s^{-1})	D_x (pc)	D_y (pc)	D_v (km s^{-1})	T_{peak} (K)	I_{int} (K km s^{-1})
a1	11.6400	42.1933	− 45.1	108.9	90.1	5.8	0.23	0.49 ± 0.05
a2	11.6203	42.1892	− 44.9	111.4	163.1	5.2	0.06	0.12 ± 0.02
b1	11.3861	41.9867	− 53.3	102.7	64.1	5.7	0.11	0.25 ± 0.03
b2	11.3880	41.9841	− 45.3	87.3	74.7	5.5	0.12	0.28 ± 0.03
b3	11.4001	41.9721	− 49.5	84.9	83.0	6.4	0.09	0.34 ± 0.04
b4	11.3892	41.9727	− 48.9	84.5	88.5	5.1	0.08	0.25 ± 0.03
c1	11.1425	41.8794	− 96.6	119.1	102.2	7.3	0.31	0.87 ± 0.04
c2	11.1314	41.8772	− 95.0	57.3	115.2	5.6	0.23	0.80 ± 0.05
c3	11.1637	41.8827	− 99.1	147.4	108.4	7.8	0.19	0.59 ± 0.05
c4	11.1779	41.8738	− 94.0	72.6	86.5	6.7	0.17	0.64 ± 0.04
c5	11.1493	41.8607	− 116.5	73.8	71.7	6.5	0.13	0.48 ± 0.04
c6	11.1461	41.8776	− 88.4	86.3	81.6	6.7	0.07	0.20 ± 0.03
c7	11.1548	41.8851	− 110.4	88.1	93.3	7.1	0.11	0.29 ± 0.04
d1	11.2350	41.9257	− 81.2	139.9	107.9	9.3	0.49	1.88 ± 0.05
d2	11.2471	41.9193	− 83.5	119.2	85.8	8.7	0.23	0.63 ± 0.04
d3	11.2653	41.9189	− 79.5	106.7	109.5	7.6	0.14	0.62 ± 0.04
d4	11.2604	41.9240	− 74.7	100.5	101.6	7.6	0.16	0.45 ± 0.03
d5	11.2266	41.9176	− 81.8	78.6	152.9	11.6	0.09	0.34 ± 0.04
d6	11.2541	41.9306	− 71.3	104.7	125.5	7.3	0.07	0.19 ± 0.03
e1	11.1074	41.6287	− 55.5	136.4	111.4	12.8	0.22	0.75 ± 0.04
f1	10.7719	41.4064	− 88.1	118.2	87.4	15.1	0.10	0.42 ± 0.04
f2	10.7804	41.4099	− 68.6	122.6	81.1	8.5	0.08	0.31 ± 0.04
f3	10.7631	41.4089	− 88.2	89.8	68.8	19.9	0.05	0.22 ± 0.03
g1	10.5999	41.1103	− 514.1	92.2	129.4	12.5	0.04	0.13 ± 0.03
g2	10.5875	41.0921	− 508.7	107.4	116.9	7.0	0.04	0.13 ± 0.03
g3	10.5860	41.1143	− 576.5	157.7	145.8	5.5	0.02	0.04 ± 0.02
h1	11.0156	41.7101	− 81.2	118.1	139.0	10.1	0.05	0.13 ± 0.03
i1	11.0545	41.5728	− 82.8	101.7	95.1	9.0	0.26	0.78 ± 0.04
i2	11.0425	41.5856	− 95.2	75.5	84.0	6.9	0.10	0.37 ± 0.03
i3	11.0536	41.5835	− 91.5	93.7	121.0	12.0	0.13	0.71 ± 0.05
i4	11.0514	41.5893	− 79.0	129.4	90.0	9.9	0.11	0.54 ± 0.04
i5	11.0607	41.5924	− 93.1	142.3	92.8	10.9	0.12	0.59 ± 0.05
i6	11.0448	41.5989	− 98.0	74.4	94.0	9.0	0.08	0.38 ± 0.04
i7	11.0631	41.5901	− 104.0	86.2	105.1	10.2	0.06	0.24 ± 0.04
i8	11.0490	41.5948	− 90.1	85.0	121.1	7.9	0.10	0.32 ± 0.04
j1	11.3529	41.7552	− 86.0	103.0	101.8	7.1	0.32	0.72 ± 0.04
j2	11.3650	41.7479	− 93.6	98.6	91.9	8.4	0.18	0.78 ± 0.05
j3	11.3694	41.7574	− 94.4	94.8	89.2	7.3	0.19	0.68 ± 0.04
j4	11.3705	41.7505	− 78.0	87.5	105.7	7.8	0.15	0.45 ± 0.03
j5	11.3773	41.7580	− 87.3	117.3	40.5	9.2	0.10	0.50 ± 0.03
j6	11.3651	41.7314	− 96.9	86.6	73.8	6.9	0.17	0.74 ± 0.05
j7	11.3763	41.7511	− 86.6	78.4	89.1	7.5	0.08	0.31 ± 0.03
j8	11.3538	41.7411	− 95.9	115.1	104.7	8.7	0.11	0.50 ± 0.04
j9	11.3438	41.7504	− 92.2	93.0	76.6	5.8	0.09	0.30 ± 0.03
k1	10.9698	41.5649	− 113.9	88.9	114.3	9.7	0.13	0.45 ± 0.04
k2	10.9511	41.5558	− 115.0	68.4	61.3	6.6	0.06	0.26 ± 0.03
R1	11.1832	41.4663	− 185.5	124.5	109.3	10.1	0.45	1.42 ± 0.04
R2	11.1913	41.4590	− 191.3	115.1	87.2	11.3	0.21	1.07 ± 0.04
R3	11.1584	41.4205	− 202.3	138.9	103.9	10.1	0.22	0.78 ± 0.04
R4	11.1702	41.4218	− 202.9	108.0	86.5	11.8	0.15	0.58 ± 0.03
R5	11.1787	41.4345	− 190.7	86.4	82.0	6.7	0.14	0.52 ± 0.03
R6	11.2097	41.4927	− 158.7	75.2	53.7	6.9	0.21	0.83 ± 0.06
R7	11.1953	41.4452	− 213.1	99.7	76.1	4.4	0.15	0.34 ± 0.03
R8	11.1714	41.4401	− 189.3	75.5	78.7	6.5	0.11	0.42 ± 0.03
R9	11.1700	41.4489	− 191.0	90.2	84.3	7.5	0.11	0.56 ± 0.03
R10	11.1413	41.4847	− 175.9	139.6	82.0	5.7	0.11	0.34 ± 0.02
R11	11.1354	41.4262	− 206.6	88.8	103.3	7.6	0.15	0.49 ± 0.03
R12	11.2016	41.4834	− 157.6	114.6	72.7	5.0	0.11	0.41 ± 0.03
R13	11.2099	41.4646	− 179.1	97.5	89.3	6.7	0.12	0.32 ± 0.03
R14	11.1836	41.4521	− 188.9	81.4	94.3	9.3	0.11	0.57 ± 0.03
R15	11.1622	41.4549	− 192.0	107.7	73.7	7.5	0.11	0.53 ± 0.03

Table A1 *– continued*

ID	RA (J2000) (°)	Dec (J2000) (°)	v (km s^{-1})	D_x (pc)	D_y (pc)	D_v (km s^{-1})	T_{peak} (K)	I_{int} (K km s^{-1})
R16	11.1720	41.4521	− 183.5	81.7	85.7	8.4	0.09	0.46 ± 0.03
R17	11.1637	41.4648	− 189.4	95.6	105.9	4.7	0.07	0.25 ± 0.02
R18	11.2165	41.4703	− 172.4	69.3	66.3	6.7	0.08	0.29 ± 0.02
R19	11.2234	41.4758	− 174.9	93.6	83.2	6.0	0.13	0.37 ± 0.03
R20	11.2006	41.4731	− 181.3	106.6	108.6	8.9	0.10	0.42 ± 0.03
R21	11.2398	41.4753	− 202.1	159.1	125.9	3.7	0.36	0.55 ± 0.07
R22	11.1873	41.4792	− 165.1	88.7	68.4	9.1	0.09	0.33 ± 0.02
R23	11.1778	41.4788	− 181.1	109.5	94.7	9.4	0.07	0.30 ± 0.03

Note. – (1) The ID of molecular clumps within each field. (2)–(4) Coordinates of the centroid of each clump. (5)–(7) The clump size (FWHM) in three dimensions, calculated using the RMS deviation of each pixel centre from the clump centroid, where each pixel is weighted by the corresponding pixel data value, i.e. CO(3–2) brightness temperature. (8) Peak brightness temperature of the clump. The RMS of this value is similar to the typical RMS of each field listed in Table 1. (9) Integrated intensity of the clump ± measurement uncertainty.

[1]*School of Astronomy and Space Science, Nanjing University, Nanjing 210023, China*

[2]*Key Laboratory of Modern Astronomy and Astrophysics, Nanjing University, Nanjing 210023, China*

[3]*School of Physics & Astronomy, Cardiff University, The Parade, Cardiff CF24 3AA, UK*

[4]*Department of Physics and Astronomy, McMaster University, Hamilton, Ontario L8S 4M1, Canada*

[5]*Purple Mountain Observatory and Key Laboratory for Radio Astronomy, Chinese Academy of Sciences, Nanjing 210023, China*

[6]*Sub-Department of Astrophysics, University of Oxford, Denys Wilkinson Building, Keble Road, Oxford OX1 3RH, UK*

[7]*Yonsei Frontier Lab and Department of Astronomy, Yonsei University, 50 Yonsei-ro, Seodaemun-gu, Seoul 03722, Republic of Korea*

[8]*Department of Astronomy, Yonsei University, 50 Yonsei-ro, Seodaemun-gu, Seoul 03722, Republic of Korea*

[9]*Department of Physics and Astronomy, Macquarie University, Balaclava Road, Sydney NSW 2109, Australia*

[10]*Research Centre for Astronomy, Astrophysics and Astrophotonics, Macquarie University, Balaclava Road, Sydney NSW 2109, Australia*

[11]*International Space Science Institute–Beijing, 1 Nanertiao, Zhongguancun, Hai Dian District, Beijing 100190, China*

[12]*Astrophysics Research Institute, Liverpool John Moores University, IC2, Liverpool Science Park, 146 Brownlow Hill, Liverpool L3 5RF, UK*

[13]*Yunnan Observatories, Chinese Academy of Sciences, 396 Yangfangwang, Guandu District, Kunming 650216, China*

[14]*Chinese Academy of Sciences South America Center for Astronomy, National Astronomical Observatories, Chinese Academy of Sciences, Beijing 100012, China*

[15]*Departamento de Astronomía, Universidad de Chile, Casilla 36-D, Santiago, Chile*

[16]*Instituto de Física y Astronomía, Universidad de Valparaíso, Avda. Gran Bretaña 1111 Valparaíso, Chile*

[17]*CAS Key Laboratory for Research in Galaxies and Cosmology, Department of Astronomy, University of Science and Technology of China, Hefei 230026, China*

[18]*School of Astronomy and Space Science, University of Science and Technology of China, Hefei 230026, China*

[19]*European Southern Observatory, Karl-Schwarzschild-Strasse 2, Garching D-85748, Germany*

[20]*Academia Sinica, Institute of Astronomy and Astrophysics, 11F Astronomy-Mathematics Building, NTU/AS campus, No. 1, Section 4, Roosevelt Rd., Taipei 10617, Taiwan*

[21]*Department of Physics and Astronomy, University College London, Gower Street, London WC1E 6BT, UK*

[22]*National Optical Astronomy Observatory, 950 N. Cherry Avenue, Tucson, AZ 85719, USA*

[23]*Astronomical Observatory Institute, Faculty of Physics, Adam Mickiewicz University, ul. Słoneczna 36, PL-60-286 Poznań, Poland*

[24]*East Asian Observatory, 660 N. A'ohōkū Place, University Park, Hilo, HI 96720, USA*

[25]*Xinjiang Astronomical Observatory, Chinese Academy of Sciences, 830011 Urumqi, China*

[26]*Max Planck Institute for Astronomy (MPIA), Königstuhl 17, D-69117 Heidelberg, Germany*

[27]*Centre for Astrophysics Research, University of Hertfordshire, College Lane, Hatfield AL10 9AB, UK*

[28]*Sterrenkundig Observatorium, Universiteit Gent, Krijgslaan 281, B-9000 Gent, Belgium*

[29]*National Astronomical Observatory of China, 20A Datun Road, Chaoyang District, Beijing 100012, China*

This paper has been typeset from a TEX/LATEX file prepared by the author.